

Geomorphic constraints on the active tectonics of southern Taiwan

Lucy A. Ramsey,^{1,3} Richard T. Walker² and James Jackson¹

¹Bullard Laboratories, Madingley Road, Cambridge, CB3 0EZ, UK

²Department of Earth Sciences, University of Oxford, Parks Road, OX1 3PR, UK

³BG Group, Thames Valley Park, Reading, Berkshire, RG6 1PT, UK. E-mail: Lucy.Ramsey@bg-group.com

Accepted 2007 March 16. Received 2007 March 16; in original form 2006 April 20

SUMMARY

Taiwan is a region of rapid active tectonics, yet the study of the tectonic processes that shape the interior of the island is difficult due to the high rates of erosion and dense vegetation. We use digital topography to look for indications of active deformation preserved in the local geomorphology. In particular, anomalies in the regional pattern of drainage are used to infer zones of enhanced tectonic activity. The apparent anticlockwise rotation of major river systems in plan view indicates the presence of a diffuse zone of left-lateral shear running down the southeastern side of Taiwan. Asymmetries in the catchments of individual drainage basins show the influence of varying rates of uplift across southern Taiwan, with the most rapid uplift close to Taitung at the indentation point of the Luzon arc with the Chinese continental margin. Our interpretations, though based predominantly on remote-sensing observations, are consistent with the available field evidence. This study demonstrates the usefulness of drainage basins as tectonic markers in the quantification of regional strain and uplift, which may have wider applicability in other deforming parts of the world.

Key words: active tectonics, drainage anomalies, geomorphology, Taiwan.

1 INTRODUCTION

In this paper, we investigate the dynamic landscape of southeastern Taiwan with particular emphasis on irregular drainage networks and their relationship to the regional tectonics (Ramsey *et al.* 2004). The geomorphology provides the opportunity to identify active, and potentially hazardous, faults in a region of little seismicity and where field investigation is limited by dense vegetation. We exploit this opportunity through the use of digital elevation models. Our observations demonstrate the potential for using drainage basins as tectonic markers in the quantification of regional strain and uplift, which may have wider applicability in other deforming parts of the world.

The oblique convergence of the Luzon Arc and the Asian continental margin results in the southward propagation of the Taiwan orogen at a rate of between 60 and 90 mm yr⁻¹ (Fig. 1b, e.g. Davis *et al.* 1983; Byrne & Liu 2002) and allows a time for space substitution along the length of the island. At present, the onset of full-scale collision is at the southern end of the Coastal Range (Fig. 1a). This indentation point of the Luzon Arc separates the advanced stage of arc-continent collision to the north from the initial stage of arc-continent collision to the south (Huang *et al.* 1997; Chang *et al.* 2001; Huang *et al.* 2006).

In the following sections, we first provide an introduction to the geology and active tectonics of Taiwan during the initial stages of arc-continent collision, before going on to describe our observations and interpretations of drainage anomalies in the south of the island. The drainage anomalies are divided into the apparent deflection

of the major rivers in plan view (Section 4.1) and asymmetries in individual drainage basins (Section 4.2).

2 GEOLOGY AND TECTONICS

The Taiwan orogen results from the rapid and oblique convergence of the Luzon Arc, riding on the Philippine Sea plate, and the Asian continental margin (Fig. 1a) (e.g. Suppe 1980; Barrier & Angelier 1986; Teng 1990). The island links the oppositely dipping Ryukyu and Manila subduction systems and forms a linear, roughly north-south oriented mountain belt that levels out at peak elevations of around 4 km above sea level. South of Taiwan, the subduction of the Asian margin beneath the Philippine Sea plate forms an accretionary prism, potentially containing slivers of continental material (Shyu *et al.* 2005a), that is progressively uplifted above sea level as the collision propagates southwards (Fig. 1b). Northeast of Taiwan, the subduction of the Philippine Sea plate beneath the Asian margin results in backarc extension at the Okinawa Trough and collapse of the orogen.

The central segment of the Taiwan orogen has been described by some as a doubly vergent wedge (Willett *et al.* 1993). The western part of the island consists of a shallow, easterly dipping fold-and-thrust belt, in Miocene-Quaternary sediments (Davis *et al.* 1983). A metamorphosed continental margin sequence (Ernst 1983), rapidly exhumed on steep, westerly dipping faults (Willett *et al.* 2003) is exposed in the eastern part of the island. The existence and significance of the range-bounding structure in the east is a matter of debate, and other workers interpret Taiwan as a one-sided wedge with

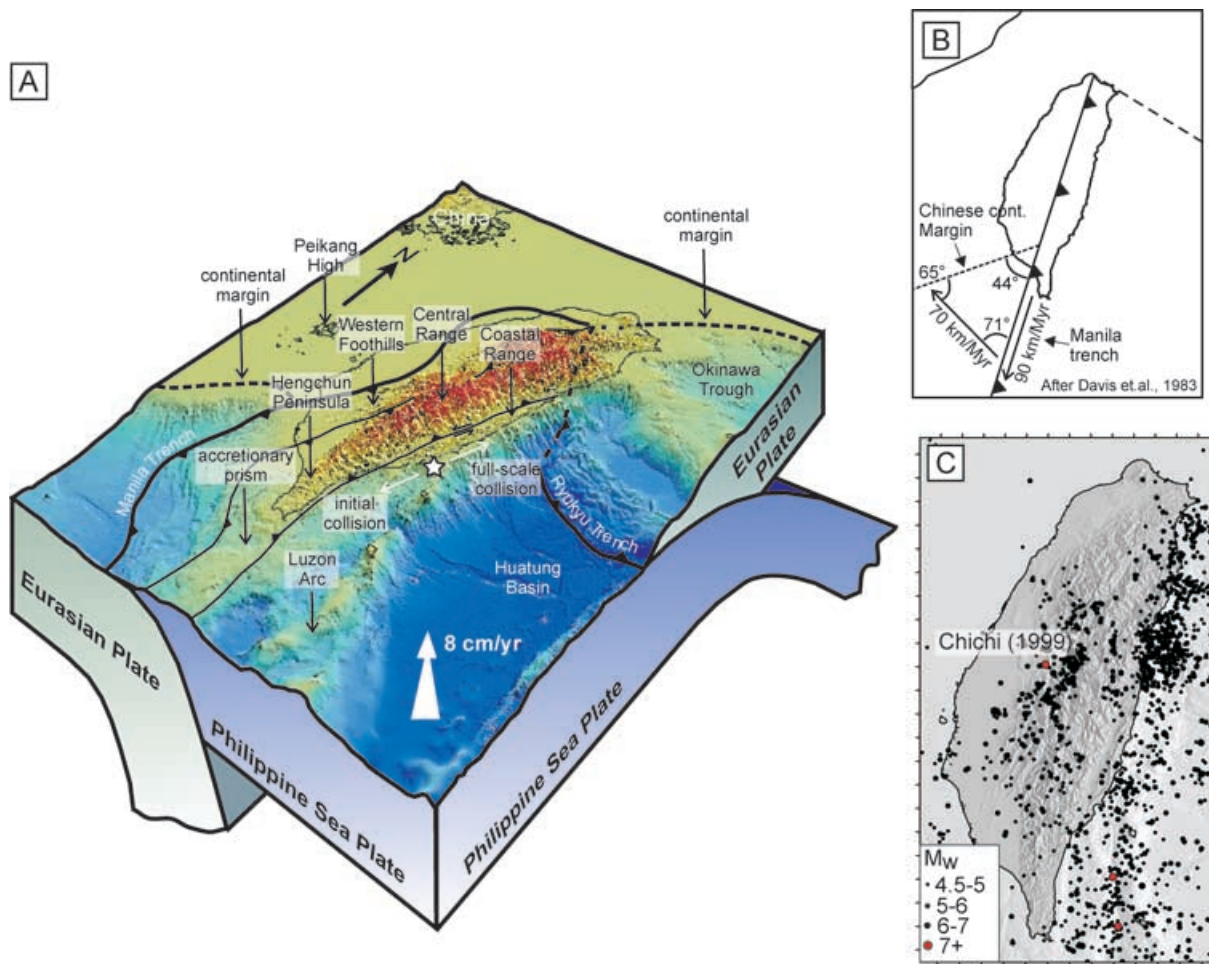


Figure 1. (a) A perspective view of the Taiwan collision and surrounding regions, looking towards the northwest. The Philippine Sea plate is moving NNW at a velocity of roughly 8 cm yr^{-1} relative to Peikang island on the Chinese continental margin. In the north, the Philippine Sea plate is subducted northwards at the Ryukyu trench. In the east, the South China Sea plate is subducted beneath the Philippine Sea plate. Taiwan is built from the collision between the Luzon arc and the Chinese continental margin, the indentation point of the Luzon Arc is shown by a white star and separates the full-scale arc-continent collision to the north from the initial stages of arc-continent collision to the south (Huang *et al.* 2006). (b) A sketch showing how the oblique collision between the Chinese continental margin and the Manila Trench-Luzon arc system results in the southward propagation of the Taiwan orogeny with a velocity of roughly 90 km Myr^{-1} . The sketch is taken from Davis *et al.* (1983). (c) The distribution of seismicity in Taiwan from the Taiwanese Central Weather Bureau catalogue.

an eastward steepening basal décollement (Suppe 1981; Davis *et al.* 1983; Carena *et al.* 2002). Regardless, the Central Range extends along the backbone of Taiwan (Fig. 1a) and is composed of bands of metasediments increasing in metamorphic grade to the west. The smaller Coastal Range bounds the east coast of Taiwan (Fig. 1a) and represents accreted segments of the Luzon volcanic arc, dominated by sandstone/mudstone rhythmites and (volcaniclastic) turbidites. Offshore to the east, the flank of the orogen descends a further 5 km and the absolute base level lies over 100 km from the coast in the Huatung basin. Offshore to the west, the orogen is flanked by a shallow marine flexural foredeep (Lin *et al.* 2003).

The Longitudinal Valley is a major tectonic suture that separates the Mesozoic metasediments of the mountainous Central Range from the turbidites and volcanics of the Coastal Range (Figs 1a and 2b) (Chang *et al.* 2001). The main Longitudinal Valley fault (Fig. 2b) follows the western edge of the Coastal Range and dips steeply to the east. In the very south of the valley, the slip is strongly partitioned between an easterly dipping thrust in the west and a north-south strike-slip fault in the east (Lee *et al.* 1998; Shyu *et al.*

2005b). The horizontal shortening in the south of the Longitudinal Valley is $\sim 22 \text{ mm yr}^{-1}$ directed at 323° (Angelier *et al.* 1997; Lee *et al.* 1998, 2001) with a roughly equal amount of vertical uplift at $22\text{--}24 \text{ mm yr}^{-1}$ (Yu and Kuo, 2001). Two large earthquakes of estimated magnitude $M_w 6.9$ and $M_w 6.8$ ruptured the central segment of the Longitudinal Valley fault and the adjacent Yuli fault in 1951 November (see Shyu *et al.* 2006a, for a detailed summary), and an earthquake of estimated magnitude $M_w 6.2$ ruptured the southern segment of the fault in 2006 April (Fig. 2b). Uplift rates for the Coastal Range determined from radiocarbon dating of Holocene marine terraces (Hsieh *et al.* 2004) show a steady increase from $2\text{--}4 \text{ mm yr}^{-1}$ in the north of the Longitudinal Valley to $6\text{--}8 \text{ mm yr}^{-1}$ in the south, punctuated by a number of anomalously low values (Fig. 2b). The pattern illustrates the culmination of the collision at the indentation point of the Luzon Arc and is in good agreement with longer term uplift rates of $>5\text{--}7 \text{ mm yr}^{-1}$ over the last $\sim 1 \text{ Ma}$ (Lundberg & Dorsey 1990). Unfortunately, there are no well-formed marine terraces between the southern end of the Coastal Range at Taitung and the Hengchun peninsula and, hence, no uplift data for the southeast coast.

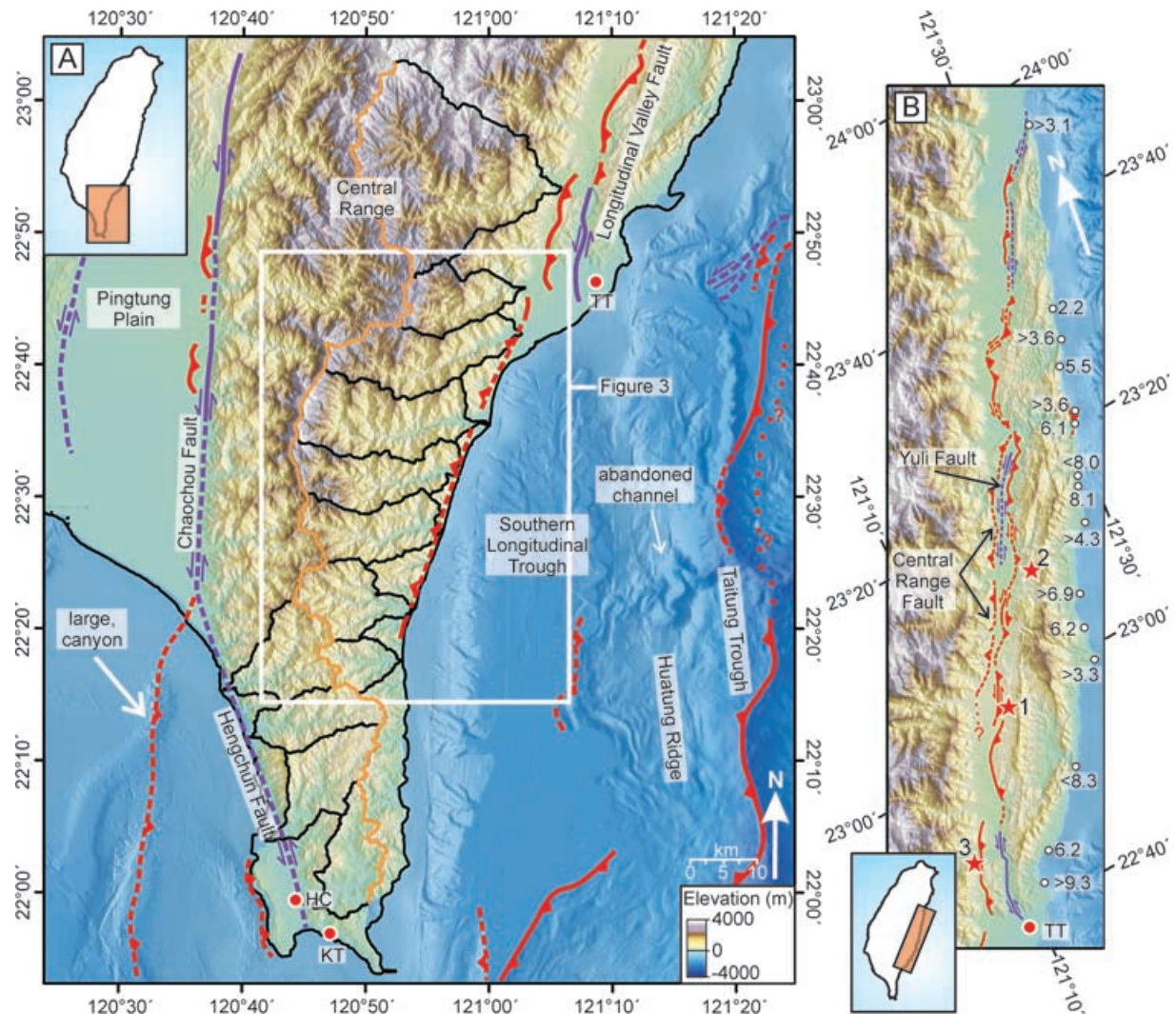


Figure 2. (a) A base map showing the topography (40 m resolution) and bathymetry (100 m resolution) of the south of Taiwan including the major active faults as proposed by Shyu *et al.* (2005b) and the main drainage divide (orange). The white box shows the extent of Figs 3(a) and (b). (b) A map showing the topography of the Coastal Range and Longitudinal Valley region and the major faults as proposed by Shyu *et al.* (2006a). The Longitudinal Valley fault follows the western margin of the Coastal Range. Other faults are named on the figure. Stars 1 and 2 mark the epicentres of the two large earthquakes of 1951 November. Star 3 marks the epicentre of the 2006 April 1 earthquake, M_w 6.2, that ruptured the southern part of the fault. The white dots and numbers are uplift rates (mm yr^{-1}) along the coast, taken from Hsieh *et al.* (2004), note the general increase in uplift rate southwards.

Other major structures in the Longitudinal Valley region include the Central Range fault, a westerly dipping backthrust bounding the Central Range along the western edge of the Longitudinal Valley (Biq 1965; Shyu *et al.* 2006b). The quantitative role of the Central Range fault is not yet clear but the existence of the fault is observed through levelling lines, seismic refraction and fluvial terraces raised 10–100 m above modern streambeds. Offshore to the east, Malavieille *et al.* (2002) identify a large west-dipping thrust from bathymetric data. They suggest this thrust is the principal fault of the Coastal Range region, although this seems unlikely given the high rate of seismic and aseismic motion and the clear geomorphic expression of the Longitudinal Valley fault.

The southeastern front of the Hengchun Peninsula is marked by a sharp linear coastline (Fig. 2a) controlled by a west-dipping thrust that appears continuous with small alluvial fan scarps southwest of Taitung (Shyu *et al.* 2005b). The rate of motion on the thrust is unknown and, apart from a poorly located event of surface wave magnitude (M_s) 7.2 in 1936, there are only small-scattered earthquakes

in the region (Fig. 1c). Offshore to the east, Shyu *et al.* (2005b) map a number of active thrusts that bound the Huatung Ridge and Taitung Trough and are observed in the bathymetric data (Fig. 2a). The structures accommodate roughly half of the total present day convergence between the Philippine Sea Plate and Eurasian margin and are presumably a precursor to the shortening structures of the Longitudinal Valley further north.

On the western coast of the Hengchun Peninsula two major faults have been identified, the Chaochou fault and the Hengchun fault (Fig. 2a). The Chaochou fault trends north–south and separates the high Central Range from the Pingtung Plain. The fault dips steeply to the east and has a significant component of vertical (up on the east) and strike-slip motion (perhaps as much as 10 km of sinistral slip) partitioned between separate splays at several locations along the fault (Shyu *et al.* 2005b). There has been little historical seismicity recorded in the area, and 5 yr of GPS measurements have failed to record much localized aseismic movement across the fault, implying that it was locked over the survey period (Hu *et al.* 2004).

Shyu *et al.* (2005b) suggest the Chaochou fault is capable of producing an earthquake of moment magnitude (M_w) 7.2 and poses a significant seismic threat to the region. It is unclear whether the structure continues southwards as the Hengchun fault (Wu 1978; Ho 1988) or runs offshore along the length of a large submarine canyon (Malavieille *et al.* 2002).

3 DATA AND METHODS

The topography of the subaerial Taiwan mountain range is described by a photogrammetrically derived DEM with 40×40 m grid cells and a vertical resolution to within a few metres depending upon the terrain. The DEM is continuous across Taiwan, although there are some obvious errors during edge matching.

The synthetic drainage network determines the likely downstream route taken by water and sediment over a digital representation of the topography (i.e. the DEM). In this study, the drainage network for Taiwan was extracted from the DEM by a series of flow-routing commands. The flow direction grid determines the direction of steepest descent. The grid was created by calculating the steepest downhill slope within a window of 3×3 grid cells (the D8 algorithm; O'Callaghan & Mark 1984). For display purposes, the threshold drainage area was set at 1 km^2 . This synthetically extracted drainage network compares favourably with hydrographic maps and with drainage evident in Landsat and ASTER imagery. The maps are displayed in the local transverse Mercator Taiwan projection TWD67, Hu-Tzu-Shan datum, spheroid International 1967.

4 DRAINAGE ANOMALIES

We now turn our attention to the regular transverse rivers of the southeast coast of Taiwan (Fig. 3) to test our ability to infer tectonic processes from the geomorphology. The seven drainage basins of interest lie to the south of the Longitudinal Valley, prior to the onset of advanced arc-continent collision, and span over 60 km along the coast, equivalent to ~ 1 Myr in time (see Section 1). Their outlets drain abruptly into the Southern Longitudinal Trough offshore (Fig. 2a). The seven basins show two unusual features; there is a gradual deflection of the river outlets to the north accompanied by a systematic increase in catchment asymmetry (see Fig. 3b). In this section, we quantify these drainage anomalies and attempt to show that basin asymmetry reveals differential north–south uplift and that northward deflection of the river outlets is indicative of distributed shear. There are few other examples from the literature where river basins have been used to quantify tectonic processes (e.g. Wallace 1978; Leeder & Jackson 1993; Hallet & Molnar 2001). Prior to a detailed discussion of the two drainage anomalies, we present a brief description of the topographic growth of the Central Range to the north.

The 16 river basins that drain eastwards from the main drainage divide are shown in Fig. 4(a). Swath profile I–I' (Fig. 4b) illustrates the gradual increase in mean elevation before a plateau is reached at the latitude of the Coastal Range. This increase and then levelling off in height is mirrored by the mean hillslope angle for each discrete basin (Fig. 4c), as well as for a number of other topographic attributes including range half-width and mean relief (Kitching 2002). Basins 1–7 increase their drainage area across strike by the elongation of their catchments. In contrast, basins 8–16 appear to increase their drainage area along strike by capture and expansion into neighbouring basins (for example, basins 8–10, Fig. 4a).

Many authors have suggested the attainment of 'threshold' topographic attributes is evidence of a topographic steady-state, whereby erosional efflux of material is balanced by tectonic influx. Relief is then limited by the mechanical threshold imposed by the maximum sustainable rock-slope angle, and erosional processes such as rockfalls, landsliding and glaciation all work to reduce the tectonic input of mass (Schmidt & Montgomery 1995; Whipple *et al.* 1999). The Coastal Range appears to act as a buttress to basins 8–16, preventing their continued increase in drainage area across strike and maintaining a constant range half-width. In addition, the hillslopes of the Central Range appear to have achieved their maximum slope angle along this transect (Fig. 4c) resulting in a constant catchment relief and mean elevation (Fig. 4b). Densmore *et al.* (2005) make a similar observation about catchment geometry and catchment expansion for the normal fault bounded ranges of the northeastern Basin and Range province. They suggest that once the hillslopes have reached a threshold angle, range half-width is limited by fault-spacing and the position of base level. In Taiwan, the Coastal Range backstop may be a crucial boundary condition to the attainment of topographic steady-state.

4.1 Northward deflection of rivers

4.1.1 Observations

The seven river basins of the southeast Central Range show a remarkable, systematic increase in the deflection of their drainage outlets to the north at an angle oblique to the range crest (Fig. 3b). We have measured the angle between the trend of the lower reaches of each basin and the east–west direction and present the results in Table 1 and as a graph in Fig. 3(c). The plot shows a roughly linear trend of increasing deflection with distance along the range, reaching a maximum of $\sim 30^\circ$ for basin 7 at the southern end of the Longitudinal Valley. The deflection does not affect basins 1 and 2 and appears 'pinned' approximately 14 km inland along a line parallel to the coast and at the headwaters of river 7. The kink in each river valley is pronounced, the upper reaches of the catchment are perpendicular to the range crest, and there are no obvious offsets of features along the valley.

The drainage basins are simple-looking networks with typically one main trunk stream and numerous branching tributaries (Fig. 3a); the more northerly basins are elongated (basin 7 is anomalous) and have an asymmetric tributary network (described further in Section 4.2). The valley floor narrows upstream of the knickpoint (Fig. 5a), an observation also made along strike in basins 1 and 2. All seven basins show a strong modal peak in the hillslope angle–frequency plots that gradually increases from $\sim 24^\circ$ for basin 1 to $\sim 31^\circ$ for basin 7 (see Figs 4c and 5c). Several of the channel profiles show large knickpoints (Fig. 5b): the largest knickpoint at channel 6 is over 200 m high and coincides with the deflection point in the basin shape.

The digital elevation data set can be manipulated to produce a map of local relief map (Figs 6a and b). The map is produced by joining the ridge crests of the interfluvies and valleys parallel and perpendicular to the range crest and producing a grid of local maximum elevations (as shown schematically in Fig. 6c). The difference in elevation between the present-day topography and the smoothed approximation of ridgelines leaves a grid of the minimum amount of sediment removed in that landscape, a measure of local relief. Ridge crests will tend to show low sediment removal (blue in Fig. 6a) and valley floors will show high sediment removal (red in this case).

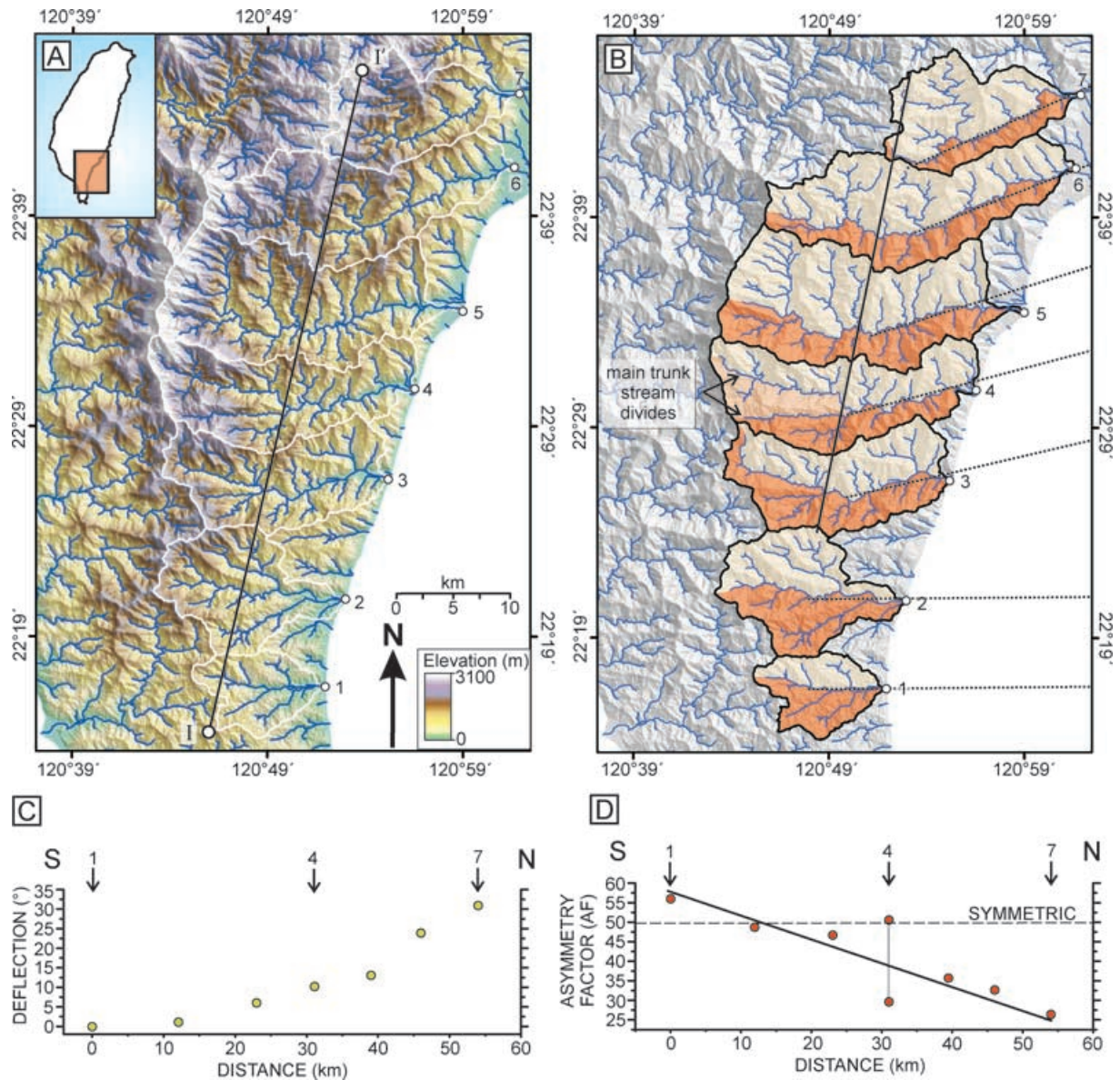


Figure 3. (a) 40 m DEM of the seven regular basins along the southeastern Central Range. The drainage area of each basin is shown by a thin white line and the outlet of each basin by a small white circle. The synthetic drainage network is shown in blue. (b) Shaded topography with basins 1–7 outlined in black and the synthetic drainage network shown in blue. The solid black line marks a change in trend of the main trunk streams and the dotted black lines mark the general trend at the outlet of each river. Note the systematic northwards deflection of the drainage outlets from basin 1 to 7 and the increasing asymmetry in catchment area north and south of the main trunk streams. The southern drainage area of each catchment has been shaded in dark orange for clarity. (c) A graph to show the increasing northward deflection of basins 1–7. The deflection is measured as the angle between east and west and the general trend of the outlet as shown in part (b). Distance is measured from outlet 1 to each subsequent outlet. Basins 1, 4 and 7 are marked for reference. (d) A graph to show the increasing asymmetry of basins 1–7. The asymmetry factor is measured using the 2-D area (see text for details). The main trunk stream of river 4 is split at the headwaters and an asymmetry factor has been given for each case.

There are two striking observations revealed by the relief map (Figs 6a and b). First, the roughly north–south deflection line observed in the digital elevation model is marked by a low in the sediment removal (along line I–I'); secondly, the upper reaches of basins 2–5 show significantly higher relief in their headwaters above the deflection line than in their lower reaches. The high relief in the headwaters of basins 2–5 is matched on the western side of the range crest by basins i–iv, so much so that the drainage divide (II–II') is partly obscured and the rivers appear continuous across it.

Looking in more detail, basin 6 shows a reversal of this pattern; the lower reaches show pulses of high relief but westwards of the

line the relief is low and uniform. The same observation can be made for basin 7, although the low in relief is in the headwaters of river iv on the eastern side of the divide in this case (Fig. 5b).

4.1.2 Interpretation and discussion

We begin our interpretation by considering the significance of the western boundary of the anomalous drainage, which is coincident with a line of low relief, across which the valley floors narrow abruptly (Figs 3b and 6a). The two most obvious causes for this sharp boundary are discussed in turn: (i) the line marks an old drainage

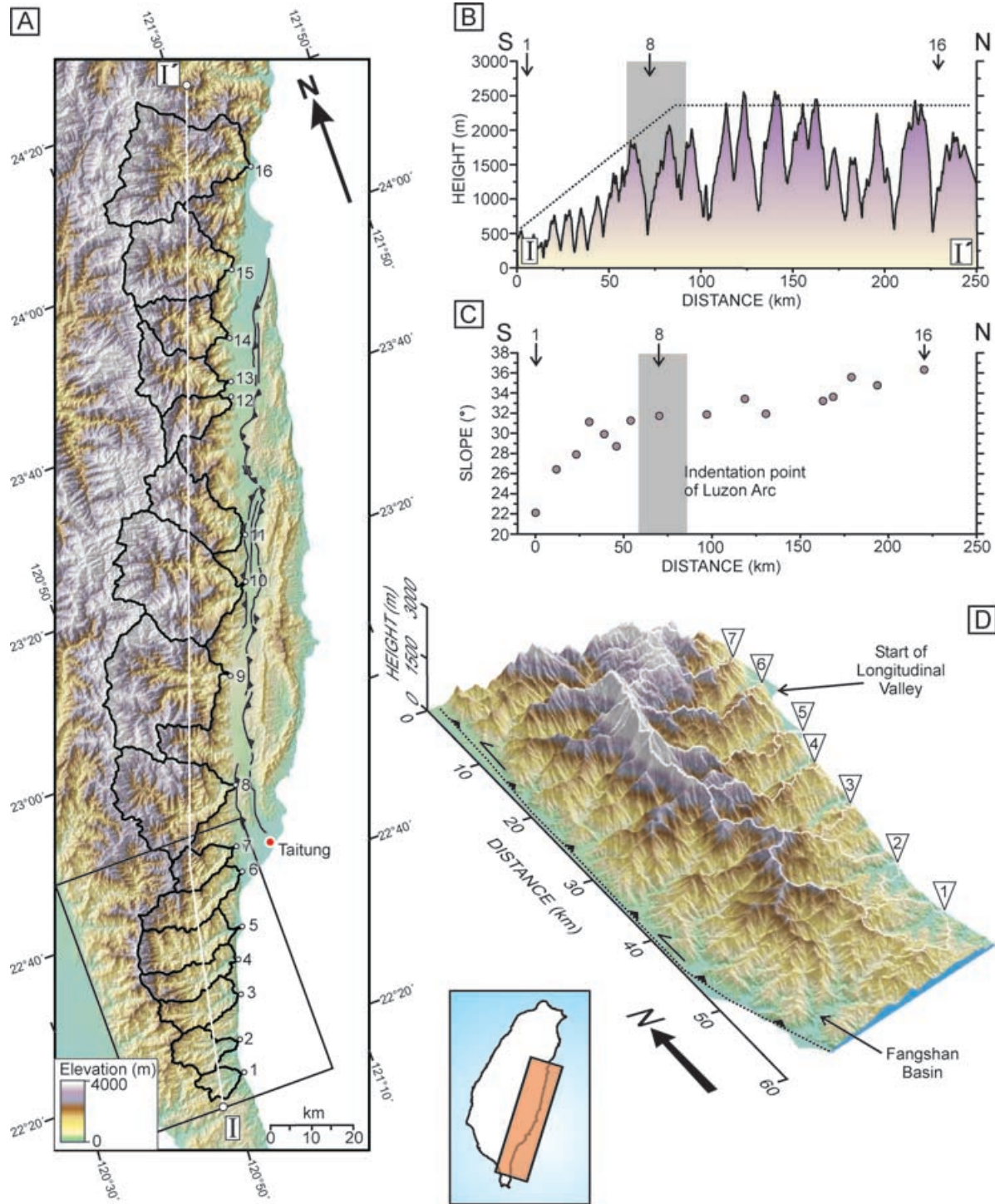


Figure 4. (a) 40 m DEM of the 16 basins along the eastern Central Range that have their headwaters at the central drainage divide. The drainage area of each basin is shown by a black line and the outlet of each basin by a small white circle. Thick solid lines represent the traces of the active Longitudinal Valley fault. The solid white line gives the position of profile line I-I' and the black box outlines the extent of part (d). (b) 5 km swath profile I-I'. The grey area marks the start of the Longitudinal Valley and the indentation point of the Luzon Arc. Basins 1, 8 and 16 are marked for reference. (c) The mean slope of the hillslopes (drainage area <math>< 1 \text{ km}^2</math>) for each drainage basin. (d) Perspective view of drainage basins 1-7. The western extent of the figure is bounded by the Chaochou Fault. Note the deflection of outlets 3-7 to the north.

divide that has recently shifted westwards, resulting in large-scale erosion in the river headwaters and (ii) the line marks a fault, and the change in uplift rate across the fault provokes a response in the headwaters of the rivers that differs from that of the lower reaches.

We then discuss the mechanism of the apparent deflection of the drainage outlets.

In the south of the Hengchun peninsula, the drainage divide is moving westwards by the progressive capture and excavation of

Table 1. The deflection and asymmetry factor for basins 1–8 (see text for details). The distance is measured from outlet 1 to each subsequent outlet.

Basin	Trunk stream	Distance (km)	Deflection (°)	Asymmetry (AF)
1	Daren	0	0	55.9
2	Dawu	12	2	48.8
3	Dazhu	23	6	46.7
4	Jinlun	31	10	50.5/29.6
5	Taimali	39	13	35.4
6	Chihpen	46	24	32.7
7	Lichia	54	31	26.4
8	Peinan	70	–	21.1

river headwaters (Ramsey *et al.* 2006). Evidence of drainage divide movement is found as far north as the upper reaches of the Fangshan basin (marked on Figs 2a and 6a), and it would not be surprising if subtle signs of divide migration were found in the seven basins discussed here. If the deflection line marked an earlier existing drainage divide, we might expect the widespread preservation of dry valleys and the early equilibration of the oldest basins (6 and 7). Rivers i, ii, iii and iv (Fig. 6a) do appear to match up in position and trend with their counterparts on the eastern flank; unfortunately, the channel profiles (Fig. 6d) show no signs of river beheading and there are very few dry valleys or wind-gaps across the divide (Fig. 6a). The oldest basin, basin 7, remains stunted and basin 6 retains a large knickpoint in the main channel profile and a low relief surface in the upper reaches. Furthermore, the sharp physical contrast in the topography at the deflection line suggests a sharp boundary at the western edge of the deformation zone, as opposed to a gradual retreat.

The second interpretation, that the deflection line follows a fault trace, is more consistent with the observations. The fault would trend NNE–SSW, in a similar orientation to the Longitudinal Valley suture and to the thrust fault bounding the peninsula. If the fault has a component of uplift a knickpoint would be produced along the river channel. The channel would respond by increasing channel incision, the hillslopes would steepen, and channel narrowing and increased sediment removal would occur; in a detachment-limited environment the knickpoint would propagate upstream (Whipple & Tucker 2002). This interpretation is compatible with the relief map (Figs 6a and b): river profile 6 has a large knickpoint at the deflection line which, as it propagates upstream, will increase sediment removal behind it. A wave of erosion may already have passed up channels 3–5, so that what we are seeing is the increased sediment removal upstream of the knickpoint, and not the knickpoint itself. There is only limited seismicity in the area (Fig. 1c). A fault is marked along the deflection line on the geological map although it is not clear what evidence was seen in the field. If the deflection line represents a fault, it is unlikely to possess a large lateral component as localized strike-slip would result in abrupt deflections within the deeply entrenched channels of the rivers which cross it.

On turning our attention to the cause of the deflection itself, one of the most compelling observations is the gradual, and apparently smooth, northward increase in deflection of the outlets. There is no systematic climatic or lithologic control on the southeast coast of Taiwan that could explain this continuous pattern, and we must turn to tectonics as the cause. The identification of active faults is made difficult by the dense vegetation and a lack of seismicity; the GPS network and any exhumation or age control data are sparse in this

area. Nevertheless, a consideration of the structures and tectonic framework may still provide clues to account for the deformation.

Recent work by Lu *et al.* (2001, 2002) has mapped the structures along the southeast coast. They characterize a series of synclinal and anticlinal folds parallel to the seven drainage basins. They also describe evidence for pervasive roughly north–south left-lateral shear throughout the area from small left-lateral fault zones and fracture cleavage orientations. This left-lateral shear zone is likely to be associated with the Longitudinal Valley suture and the river valleys may be acting as passive markers, recording the shear as a northward deflection at their outlets (Fig. 7). If we know the rate of strike-slip motion on the Longitudinal Valley fault and the age of the river basins, we can calculate a crude estimate of the expected amount of shear.

The Longitudinal Valley suture varies from a single fault in the north to partitioned strike-slip and reverse faulting on two separate fault strands in the south (Lee *et al.* 1998) (Fig. 2b, see also Section 2). Lee *et al.* (1998) estimate a horizontal displacement rate of $\sim 28 \text{ mm yr}^{-1}$ at an azimuth N329°E between the Coastal Range and the Central Range at the base of the Longitudinal Valley. The motion is partitioned into strike-slip faulting (22 mm yr^{-1} in direction N353°E) and thrusting (12 mm yr^{-1} in direction N280°E). The coastline adjacent to drainage basins 1–6 is sharp, and is thought to represent active faulting on a west-dipping thrust (Shyu *et al.* 2005b). This inferred coastal fault is directly along strike from the Longitudinal Valley fault (Figs 2a and 7a).

Assuming that the zone of deformation that we have inferred from the deflected drainage is 14 km wide (bounded by the coastline and the deflection line), and that we know the age of basin 7, we can calculate the expected amount of shear. The propagation rate of the Taiwan collision is estimated to lie between 60 and 90 mm yr^{-1} (see Section 1), depending upon the means of estimate and the exact plate geometry. The outlet of basin 7 lies ~ 55 km from the undeformed outlet of basin 1 and, substituting time for space, gives an age range of 0.6–0.9 Myr and an expected amount of shear of between 43° and 55°. Fig. 7 shows the simple calculation for the basin at an age of 0.9 Myr. The measured deflection of basin 7 is 31° (Table 1, Fig. 3c), approaching the estimated range of 43°–55°. Any discrepancy between the observed and estimated amount of shear may result either from a change in the rate of motion on the Longitudinal Valley fault, from uncertainty in the rate of southward propagation of the Taiwan orogen, or may also be related to the long-term plastic behaviour of the sediments and the coupling between the upper crust and deformation at greater depths.

There are no obvious faults in the southeast Central Range to take up the left-lateral shear, and the dense vegetation and lack of seismicity make it difficult to assess whether such faults exist, but if they did, we might expect to see them as lateral deflections of the river channels. Significantly, the underlying lithology of basins 1–7 is low grade metasediment, typically muds with some sandstone beds, that rapidly gives way to more competent marbles and schists further north. Given the widespread presence of weak mudstone rocks, pervasive shear throughout the zone appears to be a plausible mechanism. However, it is possible that the seven rivers themselves trace fault lines and that the shear is being taken up by a number of individual blocks that rotate anticlockwise about a vertical axis.

In summary, the seven basins of the southeastern coast may be considered as markers illuminating the left-lateral shear of the Taiwan collision (Fig. 8). The left-lateral shear occurs within a zone ~ 14 km wide and bounded by faults on both its coastal and inland margins.

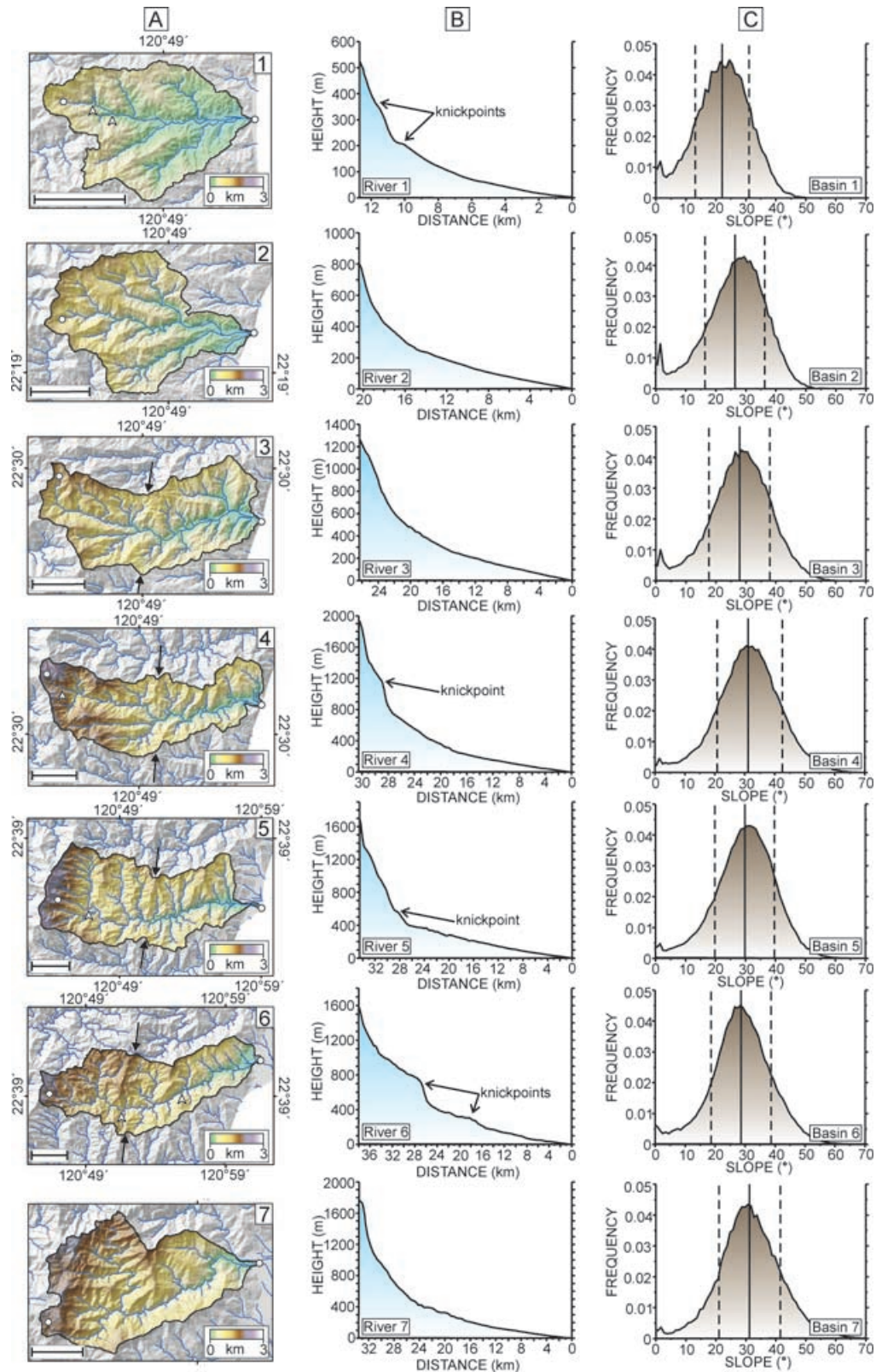


Figure 5. (a) 40 m DEM of each of the seven river basins (labelled in the top-right corner) draped over the shaded topography. The outline of the basin is shown in black and the synthetic drainage network in blue. The start and end of the river profiles in part (b) are shown by a white dot and the position of the knickpoints by white arrowheads. The knick in the river basin trend is shown by two black arrows. The scale bar is 5 km long in each case. (b) River profiles taken from the 40 m DEM and smoothed by 7 point adjacent averaging. The profile is for the main trunk stream in each basin and the headwaters and outlets are marked by a white dot in part (a). Note the large knickpoints in the upper reaches of four of the basins. (c) Slope frequency distributions for the hillslopes (drainage area <math>< 1 \text{ km}^2</math>) of each basin. The mean value and one standard deviation are shown by the solid and dotted lines respectively. Note the gradual shift to higher modal and mean slopes from basin 1 to 7.

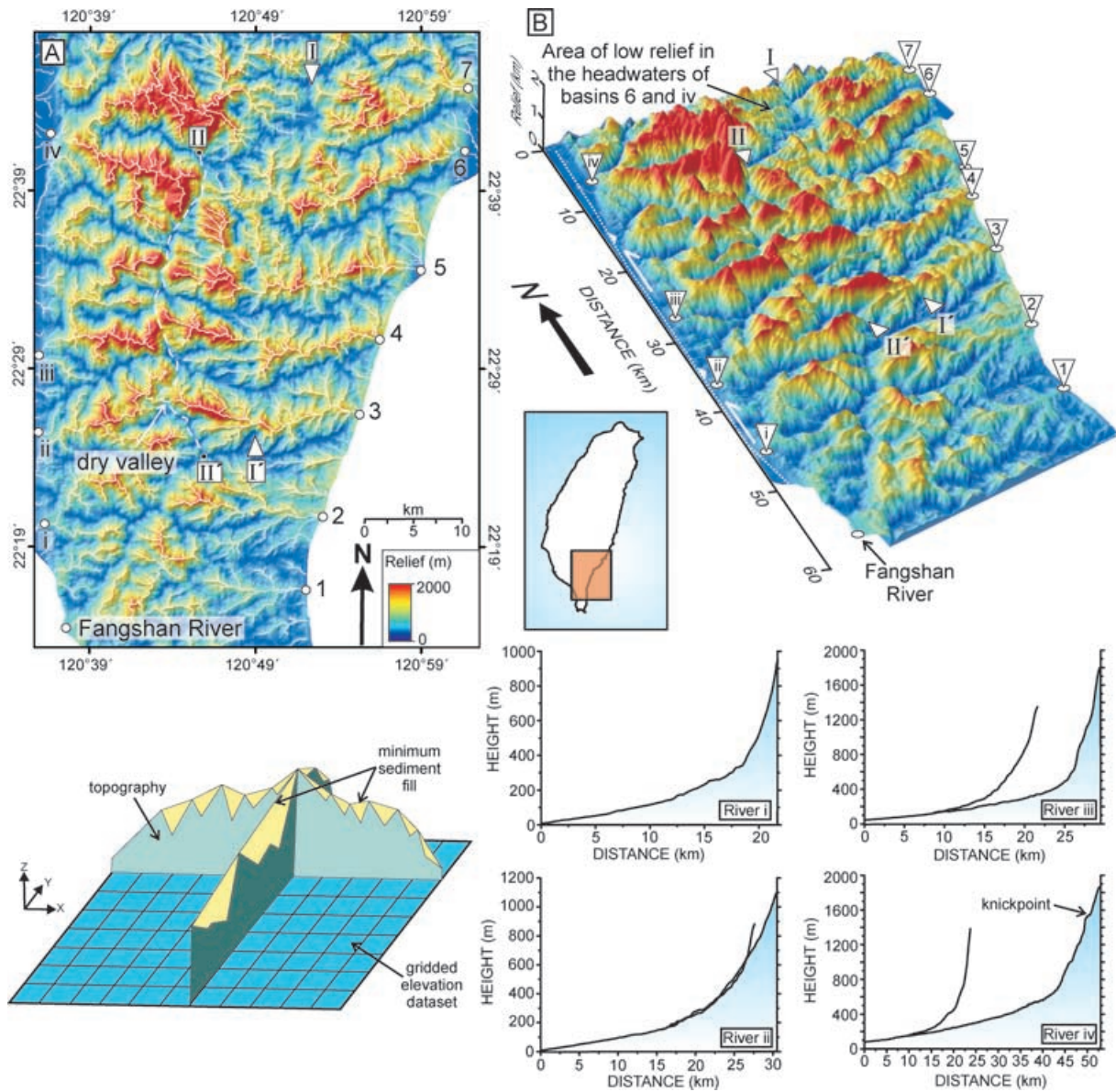


Figure 6. (a) Plan view of local relief map showing the minimum sediment removal for the southeastern Central Range. See part (c) and text for more details. The low in relief that coincides with the deflection line is marked by arrows I–I' and present-day drainage divide is marked by the white dotted line II–II'. Note the high levels of sediment removal in the headwaters of rivers 3–5 and their continuation westwards into basins i–iv. (b) Perspective view of the same area looking northwards. The western extent of the figure is bounded by the Chaochou fault. (c) A schematic figure illustrating how the relief map is generated. The topography is 'filled' (yellow) to a maximum level in a specified window size. The true topography is removed from the filled grid to give the minimum sediment fill, following the method of Brozović *et al.* (1995). (d) Channel profiles from rivers i, ii, iii and iv. The main trunk stream is shaded in blue and any large tributaries shown by a single black line. The river profiles are not obviously beheaded and there is only one significant knickpoint in the upper reaches of basin iv, coincident with the area of low relief.

4.2 Catchment asymmetry

The series of seven drainage basins described in Section 4.1 also show a striking asymmetry in their catchment areas north and south of each trunk stream. The asymmetry is clear in plan view (Figs 3b and 9a) and in topographic profiles (Fig. 9b). The asymmetry is apparent for the entire length of each basin and becomes more pronounced in the northerly basins (the deflection line identified in Section 4.1 has no obvious effect). To the north, basin 8 also shows a strong asymmetry in its catchment area (Fig. 9d). In this section, we quantify the asymmetry in the eight basins and explore the potential for further interactions between tectonics and topography in this part of Taiwan.

4.2.1 Observations

The basin asymmetry is calculated using the asymmetry factor, AF, as defined by Hare & Gardner (1985):

$$AF = 100 (A_r / A_t), \quad (1)$$

where A_t is the drainage area of the whole catchment and A_r the drainage area to the right of the main trunk stream looking downstream, that is the area to the south of each trunk stream in this case. If the catchment is symmetric the asymmetry factor should be ~ 50 . In this study, an AF of 0 would imply the southern tributaries are non-existent, and conversely an AF of 100 would imply the northern tributaries are non-existent. We have calculated the asymmetry

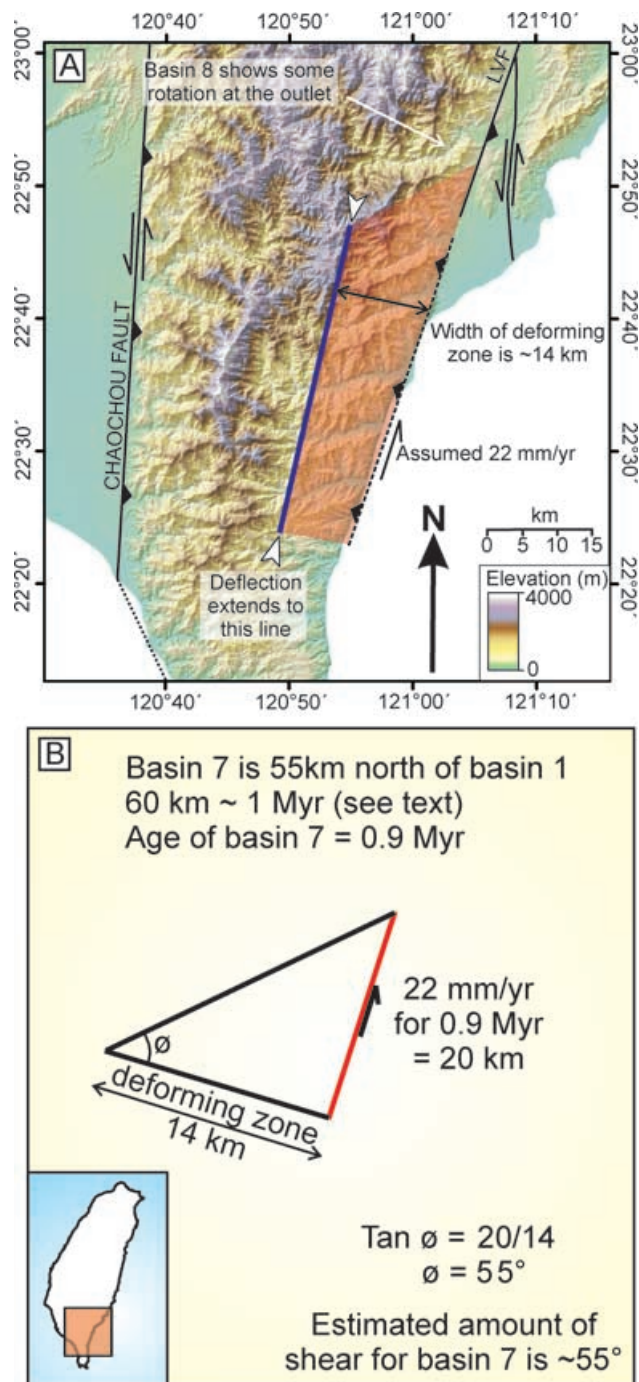


Figure 7. (a) 40 m DEM delineating the major bounding structures of the southeast coast and the extent of the shear zone (semi-transparent orange box). The known faults are shown by black lines (LVF = Longitudinal Valley fault) and the proposed faults are shown in dark blue. (b) The relationship between the left-lateral shear, the width of the deforming zone and the expected amount of rotation, ψ .

factor for each of the eight basins in plan view and present the results in Table 1 and as a graph in Fig. 3d. The distance is measured from river 1 to each subsequent outlet, river 4 has no clear trunk stream and an asymmetry factor is given for both branches of the river. Basins 1, 2 and 3 have an AF of ~50; basin 4, and those further north, show a steady, roughly linear increase in AF reaching a maximum value

of 21 for basin 8 (i.e. at least $\frac{3}{4}$ of the drainage area of basin 8 is to the north of the trunk stream). The drainage network of basin 8 is more complicated than basins 1–7 (Fig. 9d). If the more northerly tributary is chosen as the main trunk stream the asymmetry factor of basin 8 would be significantly less, and the maximum AF would be 26 for basin 7.

It is also worthwhile considering the tributary pattern on moving northwards; accompanying the increase in northern catchment area is an obvious increase in hillslope length and an increase in the sinuosity of the northern tributaries. This is especially noticeable in some of the larger tributaries of basins 5–8, in particular, at the confluence with the main channel (Figs 9a and 8). The tributaries to the south of the main trunk stream are typically short, straight and closely spaced.

In addition, the network becomes rectilinear in the northern basins with all tributaries converging with the main trunk stream at almost 90°. At several points along the interfluvies, dry valleys bridge the tributaries of neighbouring basins, specifically in the upper reaches of basins 3–6 (Fig. 8), suggesting the drainage divides are not stationary.

In contrast to the tributary network geometry, the hillslope angles north and south of the trunk streams are surprisingly constant within each basin. Fig. 9(e) documents the mean hillslope angle north and south of each trunk stream for an individual basin. Despite the general increase in slope northwards the northern hillslopes are not consistently steeper or shallower than the southern hillslopes.

To summarise, basins 1–8 have an asymmetry which significantly increases northwards, the drainage network is rectilinear, the northern tributaries are longer and more sinuous than their southern counterparts, and yet the hillslope angles remain constant within a basin. The pattern is more established and extreme in the older, northern basins suggesting a process that accumulates over time. The following interpretation section discusses the possible causes and the hillslope-channel feedbacks.

4.2.2 Interpretation and discussion

Ideally, catchment areas should be symmetric about the main trunk stream suggesting they have incised a roughly horizontal surface of uniform lithology with little preferred structural orientation. In reality, common exceptions arise in regions of increasing surface elevation across the basin (e.g. Fig. 10), usually associated with tectonic uplift (e.g. Hare & Gardner 1985; Cox 1994; Jackson *et al.* 1998), or where asymmetries in lithology or local climate exist (Kennedy 1967).

In southeastern Taiwan, there is no systematic climatic or lithologic control that could result in the steady increase in asymmetry on moving northwards. Moreover, the slope angles appear roughly constant within a single basin, a geometry that is difficult to achieve via a climatic or lithologic process (Fig. 10). Instead, we need simply appeal to the incision of the river network on a landscape that is tilted up to the north and where the valley sides are controlled by a threshold process—potentially landsliding—that maintains a constant slope (Fig. 11). The tilt of the surface is brought about by the older, northern basins having been uplifted for longer.

This simple interpretation of incision on a tilted surface can be used to derive a relationship between the amount of tilt and the asymmetry factor (Fig. 11, Appendix A). If the initial cross-channel profile is symmetric and the channels are tilted up to the north there will be an immediate asymmetry imposed in plan view; the overall width of the basin will decrease and the catchments to the south of

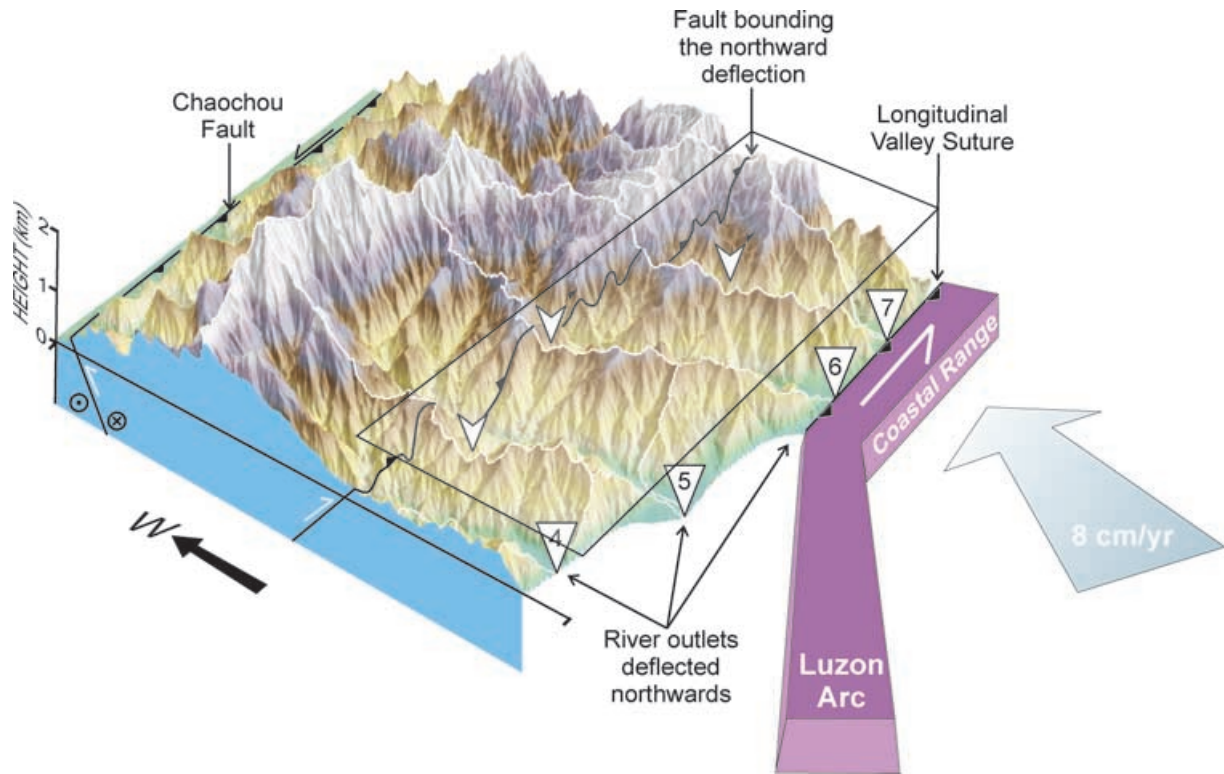


Figure 8. A cartoon illustrating the indentation of the Luzon Arc and deflection of the river outlets. Rivers 4–7 are shown by white arrowheads, the extent of the shear zone is shown by the partially transparent box. Prominent topographic lows along the interflues are marked by white arrowheads. The scene has four times vertical exaggeration and is 50 km across from west to east.

the trunk stream will appear larger (Fig. 11b). The initial width of the catchment is defined as $2w$, the initial hillslope length as h , the threshold angle at which the slopes reside as ϕ , and the tilt up to the north as θ .

The tilt to the north oversteepens the angle of the northern hillslopes to $\phi + \theta$ and understeepens the angle of the southern hillslopes to $\phi - \theta$. The hillslopes should readjust to their threshold angle, ϕ , by processes of incision and landsliding, although this has not yet been quantified in the field. The readjustment of the hillslopes increases the catchment area of the northern tributaries and decreases the catchment area of the southern tributaries (Fig. 11c). Our model is likely to oversimplify the true processes. Perhaps more realistically, critical hillslope angles are maintained on both sides of the river channel and variation in the rate of hillslope failure (as a function of the driving channel incision rate) drives the divide migration seen in Fig. 12(c). However, the differences between these two models are subtle. The asymmetry factor, AF, is calculated for the southern drainage area.

We now have a first-order relationship between the amount of tilt and the catchment asymmetry (Appendix A) and can produce a plot for a given range of hillslope angles (Fig. 12). The asymmetry factor is independent of the width of the catchment and the length of the hillslopes; only if the hillslopes are below their threshold slope will increased incision at the base of the channel lengthen the hillslopes and alter the geometry of the basin.

From Fig. 12, it is clear that for an increasing amount of surface tilt (θ), the asymmetry factor increases roughly linearly. This result is important; if the rivers were incising a uniformly tilted surface they would have the same asymmetry factor. Even if there has been no tilting of the surface, and the smooth increase in elevation of the

main drainage divide is caused simply by the northwards increase in width of the Taiwan orogen (with wider mountains able to support correspondingly higher peak elevations, e.g. Fig. 4) the asymmetry of the catchments would remain identical to the geometry shown in Fig. 11(b). For the asymmetry factor to increase northwards the tilt of the surface must increase northwards. Therefore, the tilt of the landscape is not only the result of the northern basins being older and having been uplifted for longer, but also the result of differential uplift rates between the southern tip of Taiwan and the indentation point of the Luzon Arc. At the southern tip, the shortening is accommodated as subduction, thrusting and uplift; along the length of the Longitudinal Valley any remaining oceanic crust has been consumed and the shortening must be absorbed as thrusting and uplift alone (Shyu *et al.* 2005a). To the north of the indentation point of the Luzon Arc, during the advanced stage of arc-continent collision (Huang *et al.* 2006), the uplift rate may be constant. The actual values of tilt output from the model are inconsistent with observation. An AF of 21 and a hillslope angle of 30° as is seen for basin 8, requires a surface tilted at just over 20° . A surface tilt of this amount cannot be produced between basin 8 and 1 (a distance of ~ 70 km) over the ~ 1 Myr since the area has been above sea level, assuming that the present-day uplift rate at the southern tip of the Longitudinal Valley of ~ 10 mm yr $^{-1}$ (Fig. 2b) is representative of the rate of uplift averaged over the last million years.

The cartoon in Fig. 11 assumes the position of the interflues between adjacent valleys to be stable in space, and that the valley floor shifts southwards to create the basin asymmetry. It is likely that at least some of the asymmetry is caused by movement of the divides themselves, as well as lateral movement of the river channels as they cut down. We suggest the readjustment of the northern

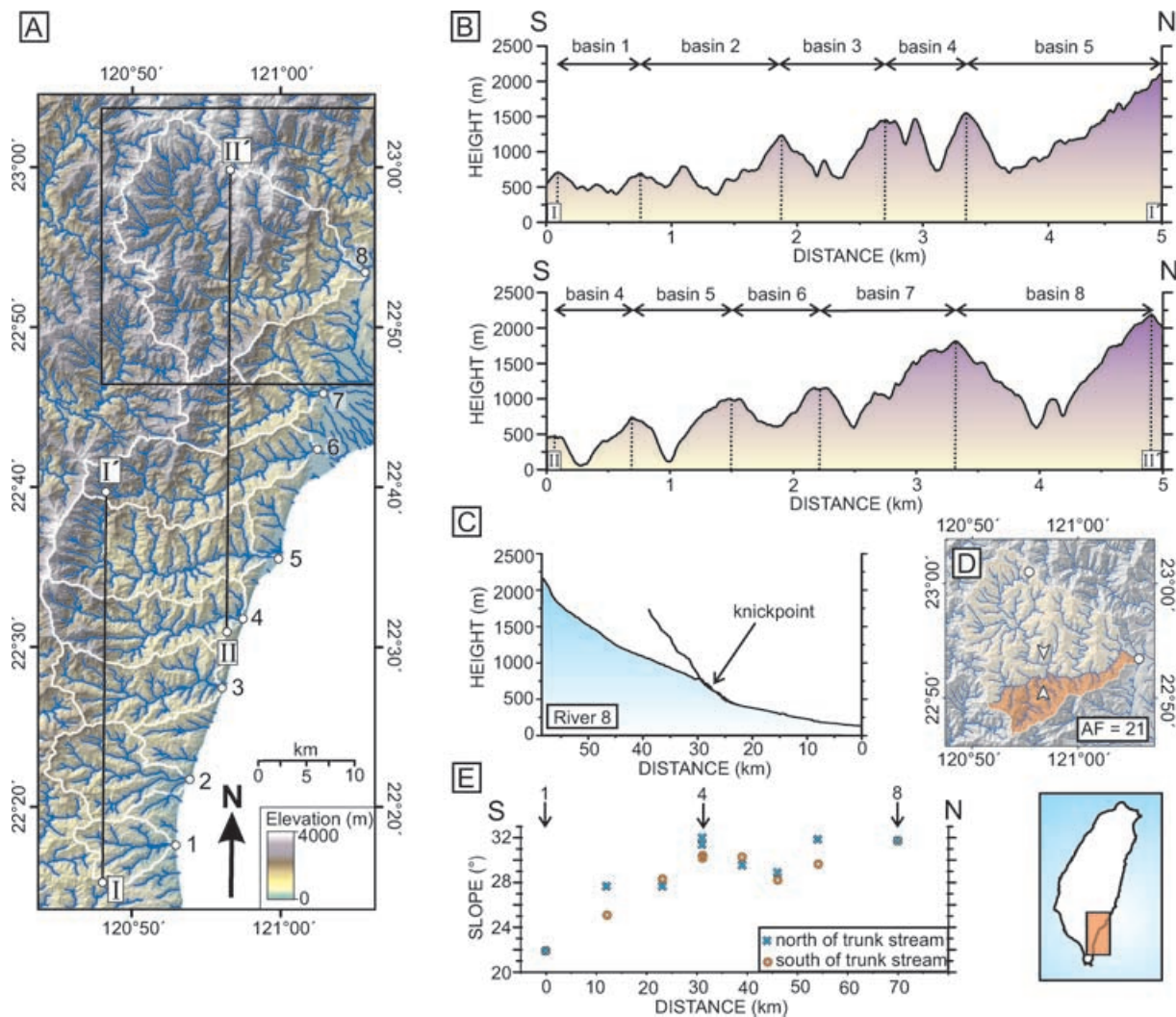


Figure 9. (a) 40 m DEM of the southeast coast including basin 8 to the north. The drainage basins are shown in white and the synthetic drainage network in blue. The black box outlines the extent of part (d) and lines I–I' and II–II' the profiles in part (b). (b) 5 km cross-valley swath profiles I–I' and II–II'. Note the offset of the trunk stream to the south of the basins in the more northerly catchments. (c) and (d) Basin 8 may form part of the large-scale trend; the channel profiles and asymmetry factor are included for completeness. The profile of the large north–south tributary is shown in blue and that of the main trunk stream by a thin black line. The white dots in part (d) mark the headwaters and outlet of the tributary; the location of the channel knickpoint is shown by two white arrowheads. AF = asymmetry factor (see text for details). (e) The mean hillslope angle north and south of each trunk stream. Basins 1, 4 and 8 are marked for reference. Note that the southern values are not systematically greater or less than the northern values.

hillslopes is manifest as landslides at the drainage divide. The northern tributaries cut back across the divide and capture the headwaters of the neighbouring southern tributaries. The continued capture shifts the drainage divide northwards. For the divides to migrate requires significant degradation along the interflues, however this is not a problem, as several kilometres of rock are likely to have been removed from this region over the past ~ 1 Myr (as discussed later). A process of northward divide migration is consistent with both the observed alignment of tributaries and the presence of topographic lows across the interflues (Fig. 8).

Both the hillslopes and the tributaries must respond to the increasing slope imposed by the differential uplift. The slope of an alluvial river bed is graded in order to maintain a delicate balance between sediment supply and removal, and the minimum amount of energy expended. Increasing a river channel gradient, even by a fraction of a degree, will cause the river to meander more, increase its length and readjust the slope to compensate. This process has

been observed for alluvial channels (e.g. Schumm 1985) but recent work has suggested bedrock meanders are equally as important and dynamic in Taiwan (Barbour *et al.* 2005). The greater sinuosity we observe in the northern tributaries may be an adjustment to the tilted surface that is concentrated at the tributary confluence before migrating upstream (Schumm 1993).

It is difficult to account for the role of denudation as a whole in shaping the basin geometry. The high uplift rates of the island of Taiwan are countered by equally high erosion rates. Apatite fission track age data from the southeast coast of Taiwan suggests exhumation rates of between 2 and 10 mm yr⁻¹ (Dadson *et al.* 2003; Willett *et al.* 2003), these are matched by river gauging station erosion estimates of 3–10 mm yr⁻¹ (Dadson *et al.* 2005). If the erosion rates have been relatively constant throughout the past 1 Myr, several kilometres of sediment may have been removed from the region. It is unlikely that sediment has been removed evenly throughout the basin, especially if uplift rates are higher in the northern basins.

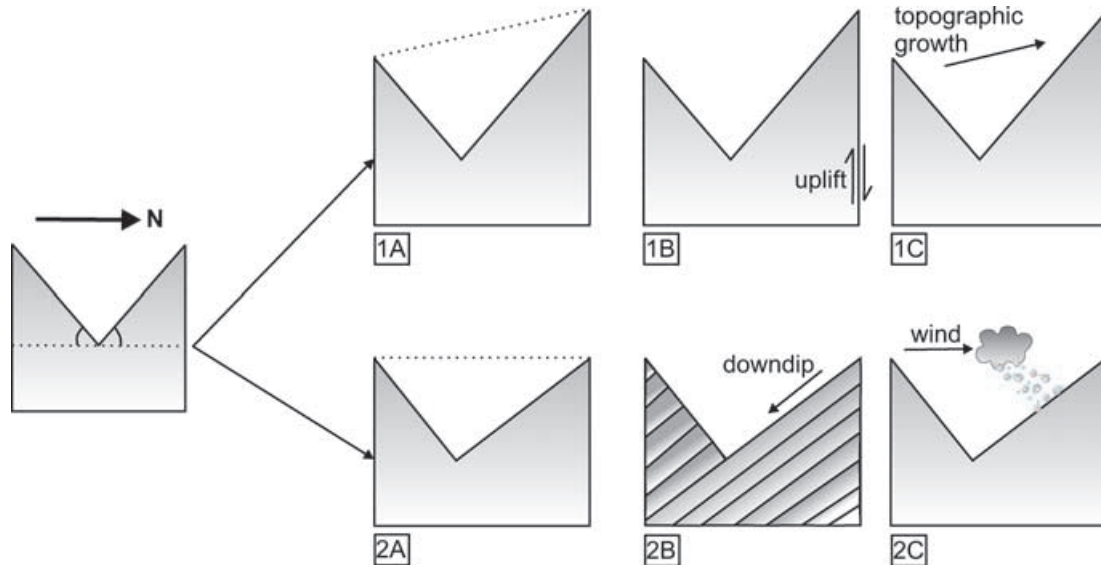


Figure 10. (a) A cartoon of river valley cross-profiles showing the development of asymmetric hillslopes. Initially the hillslopes reside at their threshold value, ϕ . Asymmetry can develop by increasing the elevation across the catchment, 1A, or by reducing the angle of the northern hillslopes, 2A. Localized faulting, 1B, or topographic growth, 1C, are possible causes of increasing elevation; the dip of the strata, a strong foliation or cleavage, 2B, or local climate variations, 2C, are possible causes of opposing hillslope angles.

A further complexity, and one that is equally difficult to incorporate in any model, is the northward linear increase in slope (Fig. 4c). If the northern basins have a steeper threshold hillslope angle they can support higher interfluvies, and the elevation will increase northwards. Moreover, if the hillslope angle is increasing rapidly northwards and the river valleys are evenly spaced, the basins could develop a marked asymmetry (Fig. 13). It is not clear why the threshold angle should increase northwards. There are no significant lithological variations shown on the geological map and the basins are uniformly underlain by low-grade Miocene sediments. There may be a more gradual increase in metamorphic grade from south to north towards the culmination of the collision, as is seen on a larger scale across Taiwan, that could result in more competent rocks in the north.

Fig. 13 has a number of implicit assumptions and important details. First, we have assumed that the incision depth remains constant between valleys, both at their outlets and along their lengths. This assumption appears to be valid in southern Taiwan as profiles drawn parallel to the coast show each river bed at roughly the same elevation (Fig. 13b). We have also assumed that the hillslopes are at their maximum sustainable rock-slope angle, and the asymmetry factor is constant for a linear increase in threshold slope. It is difficult to assess the contribution of increasing hillslope angle to catchment asymmetry. Observations suggest that the increase in threshold angle is small, especially between catchments 6–8 (Fig. 5c), yet the asymmetry continues to increase rapidly (Fig. 3b). Furthermore, the hillslope angle will no doubt increase smoothly and not remain constant within a particular basin. Nevertheless, although the signals are difficult to distinguish, it appears that the interaction of the differential uplift and increasing hillslope angle is significant.

It is perhaps surprising that catchment asymmetry is not evident in the drainage basins on the southwestern flank of the range. The western flank of the range is dominated by north–south trending anticlines in the Western Foothills fold-and-thrust belt and has a more diffuse deformational style to the eastern Central Range. The western basins are farther from the indentation point of the Luzon Arc,

the region where uplift is likely to be concentrated, and the proximity of the Chaozhou Fault may be a more important boundary condition to the drainage development. In a similar way, the asymmetry is not evident farther north along the Central Range, where one might expect the basins to record an earlier stage of deformation. The high uplift and erosion rates in the Coastal Range would rapidly remove the remnant signal.

In summary, the increasing asymmetry of the eight drainage basins is caused by the incision of river valleys in a region tilting up to the north. The uplift rate must increase northwards to the latitude of the Longitudinal Valley and is likely to be combined with an increasing threshold slope. The continuous response of the oversteepened hillslopes is to cut back by landsliding, thus capturing the drainage area of the neighbouring basin.

5 CONCLUSIONS

We have shown that the river systems of southeast Taiwan record information on the active tectonic processes that shape the orogen. Our remote sensing observations are consistent with field evidence for pervasive left-lateral shear through this part of the island. In addition, we have been able to describe both the spatial distribution and likely total magnitude of the regional strain, information that it is not possible to glean from the field observations alone. Further testing of our model could be performed by targeted GPS measurements of the present-day deformation. We have also uncovered evidence preserved within the landscape for a rapid increase in uplift rate from the southern tip of the island to the indentation point of the Luzon Arc. We have no independent geological constraints on this process. However, future measurements of the spatial pattern of erosion rate may provide independent constraints on incision, and perhaps uplift, which could be compared to our results. The rates of deformation in Taiwan are very rapid, and hence the tectonic signals retained in the rivers and landscape are very clear. However, the type of observations we have made should be applicable to any other region of

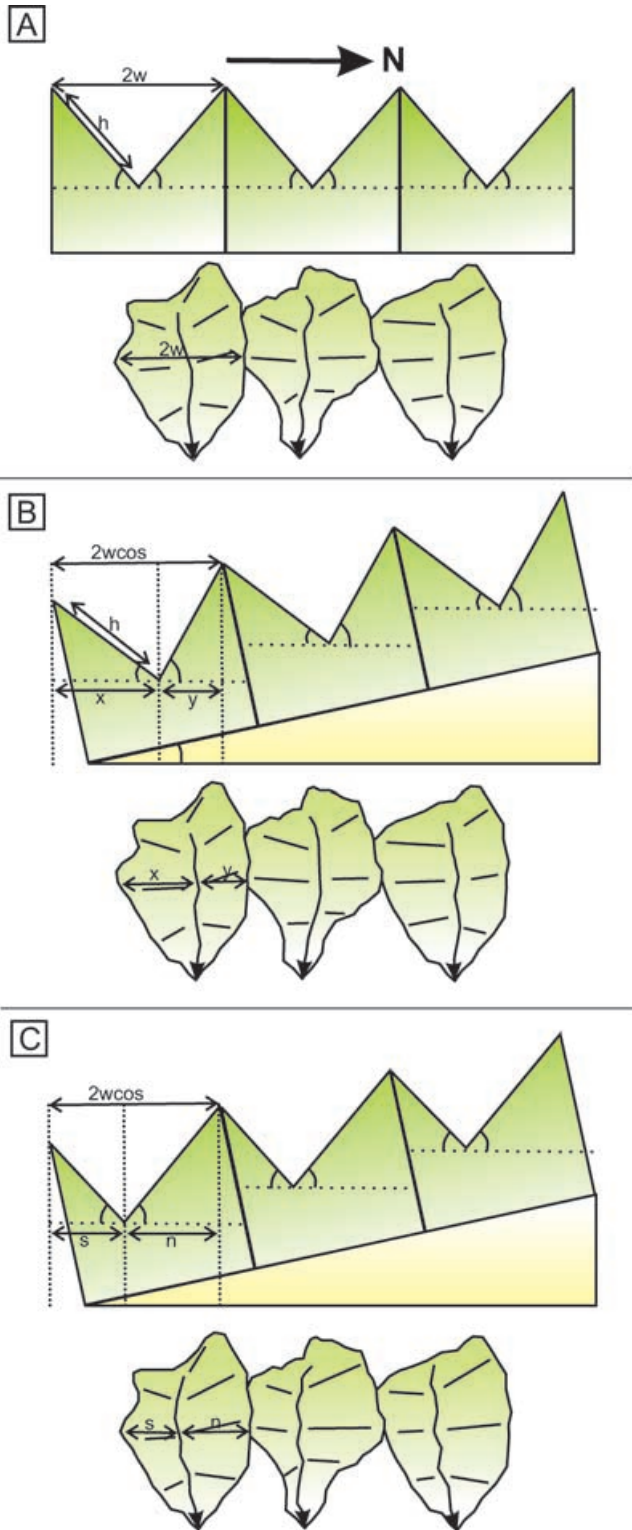


Figure 11. (a) Symmetric hillslopes in cross-sectional and plan views. (b) The asymmetry factor (AF) for a constant regional tilting of θ degrees, prior to readjustment of the hillslope angle. (c) The asymmetry factor (AF) for a constant regional tilting of θ degrees, after readjustment of the hillslope angle.

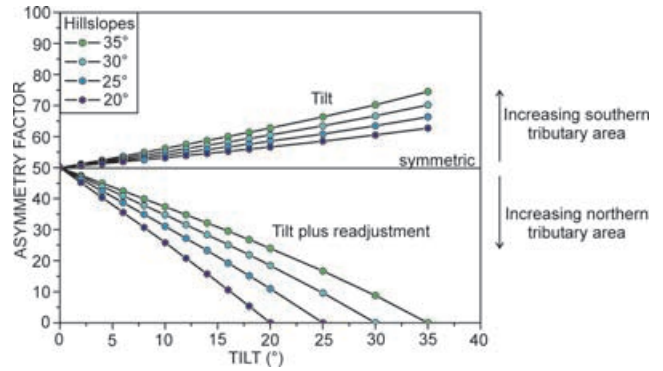


Figure 12. A plot of the expected catchment asymmetry for a given amount of tilt and a range of typical hillslope angles. The plot includes the asymmetry imposed from initial tilt of the catchments and that from tilt and readjustment of the hillslopes to their threshold angles. Note an asymmetry factor of 50 is a symmetric catchment.

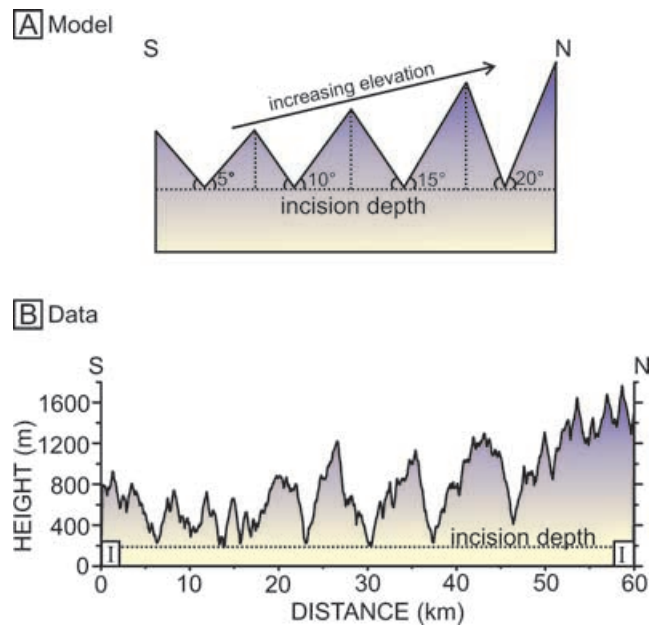


Figure 13. (a) A cartoon showing incision into a surface where hillslope thresholds increase for each subsequent basin. The rivers incise to the same depth, the interfluvial elevation increases northwards, the asymmetry of the basins is constant. (b) A topographic profile along line I-I' in Fig. 3. The rivers appear to incise to a roughly constant elevation along their base.

mountain building with along-strike variations in deformation style and rate.

ACKNOWLEDGMENTS

First, we would like to thank Prof H. Chen and family who were very supportive of our work in Taiwan. Prof Char-shine Liu provided access to the bathymetric data used in Figs 1 and 2, and Miss Char-Min provided help in organizing the logistics. This paper benefited from discussions with various people including, R. Bendick, H.-T. Chu, S.J. Dadson, A.J. Haines, N. Hovius, M.-L. Hsieh, E. Kirby, J.-C. Lee, F. Pazzaglia, J.B.H. Shyu and A.J. West. Colin Stark, Ed

Keller, Cindy Ebinger, Mike Leeder, Mike Bickle and an anonymous reviewer are all thanked for detailed comments. This is Cambridge Earth Sciences contribution No. 8766 and is supported by NERC in the form of the COMET research centre and a studentship to LAR. Additional fieldwork costs were met by Trinity College, Cambridge.

REFERENCES

- Angelier, J., Chun, H.-T. & Lee, J.-C., 1997. Shear concentration in a collision zone: kinematics of the Chihshang Fault as revealed by outcrop-scale quantification of active faulting, Longitudinal Valley, eastern Taiwan, *Tectonophysics*, **274**, 117–143.
- Barbour, J.R., Stark, C.P., Hsieh, M.-L., Hovius, N., Jen, C.-H. & Chen, M.-C., 2005. Meandering mountain rivers of the western North Pacific cyclone basin, in *European Geosciences Union General Assembly*.
- Barrier, E. & Angelier, J., 1986. Active collision in eastern Taiwan: the Coastal Range, *Tectonophysics*, **125**, 39–72, doi:10.1016/0040-1951(86)90006-5.
- Biq, C., 1965. The east Taiwan rift, *Petrol. Geol. Taiwan*, **4**, 93–106.
- Brozović, N., Burbank, D.W., Fielding, E. & Meigs, A.J., 1995. The spatial and temporal topographic evolution of Wheeler Ridge California: new insights from digital elevation data, *Geol. Soc. Am. Abstracts with Programs*, **27**, 396.
- Byrne, T. & Liu, C.S., 2002. Preface: introduction to the geology and geophysics of Taiwan, in *Geology and geophysics of an arc-continent collision*, pp. v–viii, eds Byrne, T. & Liu C.S., Geological Society of America Special Paper 358.
- Carena, S., Suppe, J. & Kao, H., 2002. Active detachment of Taiwan illuminated by small earthquakes and its control of first-order topography, *Geology*, **30**, 935–938.
- Chang, C.P., Angelier, J., Huang, C.Y. & Liu, C.S., 2001. Structural evolution and significance of a mélange in a collision belt: the Lichi Mélange and the Taiwan arc-continent collision, *Geol. Mag.*, **138**, 633–651.
- Cox, R.T., 1994. Analysis of drainage-basin symmetry as a rapid technique to identify areas of possible Quaternary tilt-block tectonics: an example from the Mississippi Embayment, *GSA Bull.*, **106**(5), 571–581.
- Dadson, S.J. *et al.*, 2003. Links between erosion, runoff variability and seismicity in the Taiwan orogen, *Nature*, **426**, 648–651.
- Dadson, S.J., Hovius, N., Pegg, S., Dade, W.B., Horn, M.-J. & Chen, H., 2005. Hyperpycnal river flows from an active mountain belt, *J. geophys. Res.*, **110**, F04016, doi:10.1029/2004JF000244.
- Davis, D., Suppe, J. & Dahlen, F.A., 1983. Mechanics of fold and thrust belts and accretionary wedges, *J. geophys. Res.*, **88**, 1153–1172.
- Densmore, A.L., Dawers, N.H., Gupta, S. & Guidon, R., 2005. What sets topographic relief in extensional footwalls?, *Geology*, **33**(6), 453–456, doi:10.1120/G21440.1.
- Ernst, W. G., 1983. Mineral paragenesis in metamorphic rocks exposed in Tailuko Gorge, Central Mountain Range, Taiwan, *Journal of Metamorphic Geology*, **1**, 305–329.
- Hallet, B. & Molnar, P., 2001. Distorted drainage basins as markers of crustal strain east of the Himalaya, *J. geophys. Res.*, **106**(B7), 13 697–13 709.
- Hare, P.H. & Gardner, T.W., 1985. Geomorphic indicators of vertical neotectonism along the converging plate margins, Nicoya Peninsula, Costa Rica, in *Tectonic Geomorphology*, chap. 4, pp. 75–104, eds Morisawa, M. & Hack, J.T., Allen and Unwin, Boston.
- Ho, C.-S., 1988. An introduction to the geology of Taiwan: explanatory text of the geologic map of Taiwan, Tech. rep., Central Geological Survey, Taiwan.
- Hsieh, M.-L., Liew, P.-M. & Hsu, M.-Y., 2004. Holocene tectonic uplift on the Huatung coast, eastern Taiwan, *Quat. Int.*, **115–116**, 47–70, doi:10.1016/S1040-6182(03)00096-X.
- Hu, J.C., Hou, C.S., Shen, L.C., Chan, Y.C., Chen, R.F., Rau, R.F., Yu, S.B. & Huang, C., 2004. Fault activity inferred from velocity of GPS measurements in the Pingtung area, southwestern Taiwan, in *Geophysical Research Abstracts*, **6**.
- Huang, C.-Y., Wu, W.-Y., Chang, C.-P., Tsao, S., Yuan, P.B., Lin, C.-W. & Kuan-Yuan, X., 1997. Tectonic evolution of accretionary prism in the arc-continent collision terrane of Taiwan, *Tectonophysics*, **281**, 31–51.
- Huang, C.-Y., Yuan, P.B. & Tsao, S.-J., 2006. Temporal and spatial records of active arc-continent collision in Taiwan: a synthesis, *GSA Bull.*, **118**(3/4), 274–288, doi:10.1130/B25527.
- Jackson, J.A., Van Dissen, R. & Berryman, K., 1998. Tilting of active folds and faults in the Manawatu region, New Zealand: evidence from surface drainage patterns, *N.Z. J. Geol. Geophys.*, **41**, 377–385.
- Kennedy, B.A., 1967. A comparative study of multiply-controlled valley asymmetry in S. E. Wyoming and S. W. Manitoba, *Master's thesis*, The University of British Columbia.
- Kitching, D.J., 2002. Time to topographic equilibrium in an active mountain belt: South Central Range Taiwan, *Master's thesis*, University of Cambridge.
- Lee, J.-C., Angelier, J., Chu, H.-T., Yu, S.-B. & Hu, J.-C., 1998. Plate-boundary strain partitioning along the sinistral collision suture of the Philippine and Eurasian plates: analysis of geodetic data and geological observation in southeastern Taiwan, *Tectonics*, **17**(6), 859–871.
- Lee, J.-C., Angelier, J., chu, H.-T., Hu, J.-C. & Jeng, F.-S., 2001. Continuous monitoring of an active fault in a plate suture zone: a creepmeter study of the Chihchang Fault, eastern Taiwan, *Tectonophysics*, **333**, 219–240.
- Leeder, M.R. & Jackson, J.A., 1993. The interaction between normal faulting and drainage in active extensional basins with examples from the Western United States and Greece, *Basin Res.*, **5**, 79–102.
- Lin, A.T., Watts, A.B. & Hesselbo, S.P., 2003. Cenozoic stratigraphy and subsidence history of the South China Sea margin in the Taiwan region, *Basin Res.*, **15**, 453–478, doi:10.1046/j.1365-2117.2003.00215.x.
- Lu, C.-Y., Chang, K.-J., Malavieille, J., Chan, Y.-C. & Chang, C.-P. and Lee, J.-C., 2001. Structural evolution of the southeastern Central Range, Taiwan, *Western Pacific Earth Sci.*, **1**(2), 213–226.
- Lu, C.-Y., Chan, Y.-C., Lee, J.-C., Chu, H.-T. & Malavieille, J., 2002. Active continental growth under transpressional tectonics—example from southeastern Taiwan, *Western Pacific Earth Sci.*, **2**(1), 37–46.
- Lundberg, N. & Dorsey, R.J., 1990. Rapid Quaternary emergence, uplift, and denudation of the Coastal Range, eastern Taiwan, *Geology*, **18**, 638–641.
- Malavieille, J. *et al.*, 2002. Arc-continent collision in Taiwan: new marine observations and tectonic evolution, in *Geology and Geophysics of an Arc-Continent collision, Taiwan, Republic of China, Geological Society of America Special Paper*, pp. 189–213, eds Byrne, T.B. & Liu, C.-S., Special Paper 358, Geological Society of America, Boulder, Colorado.
- O'Callaghan, J.F. & Mark, D.M., 1984. The extraction of drainage networks from digital elevation data, *Comput. Vision, Graphics Image Process.*, **28**, 328–344.
- Ramsey, L.A., Hovius, N., Haines, A.J. & Hu, J.-C., 2004. Entrenched transverse rivers as geomorphic strain markers: insights from south-eastern Taiwan, *EOS, Trans. Am. geophys. Un.*, **85**(47), Fall Meet. Suppl., Abstract T11D–1318.
- Ramsey, L.A., 2006. Topographic evolution of emerging mountain belts. Unpublished PhD thesis, University of Cambridge, Cambridge.
- Schmidt, K.M. & Montgomery, D.R., 1995. Limits to relief, *Science*, **270**, 617–620.
- Schumm, S.A., 1985. Patterns of alluvial rivers, *Ann. Rev. Earth planet. Sci.*, **13**, 5–27.
- Schumm, S.A., 1993. River response to baselevel change: implications for sequence stratigraphy, *J. Geol.*, **101**, 279–294.

- Shyu, J.B.H., Sieh, K. & Chen, Y.-G., 2005a. Tandem suturing and disarticulation of the Taiwan orogen revealed by its neotectonic elements, *Earth planet. Sci. Lett.*, **233**, 167–177, doi:10.106/j.epsl.2005.01.018.
- Shyu, J.B.H., Sieh, K., Chen, Y.-G. & Liu, C.-S., 2005b. Neotectonic architecture of Taiwan and its implications for future large earthquakes, *J. geophys. Res.*, **110**, B08402, doi:10.1029/2004JB003251.
- Shyu, J.B.H., Chung, L.-H., Chen, Y.-G., Lee, J.-C. & Sieh, K., 2007. Re-evaluation of the surface ruptures of the November 1951 earthquake series in eastern Taiwan, and its neotectonic implications, *J. Asian Earth Sci.*, in press.
- Shyu, J.B.H., Sieh, K., Chen, Y.-G. & Chung, L.-H., 2006b. Geomorphic analysis of the Central Range fault, the second major active structure of the Longitudinal Valley suture, eastern Taiwan, *Geol. Soc. Am. Bull.*, **118**, 11.
- Suppe, J., 1980. Imbricated structure of Western Foothills belt, southcentral Taiwan, *Petrol. Geol. Taiwan*, **17**, 1–16.
- Suppe, J., 1981. Mechanics of mountain building and metamorphism in Taiwan, *Mem. Geol. Soc. China*, **4**, 67–89.
- Teng, L.S., 1990. Geotectonic evolution of Late Cenozoic arc continent collision in Taiwan, *Tectonophysics*, **183**, 57–76.
- Wallace, R., 1978. Geometry and rates of change of fault-generated range fronts, north-central Nevada, *J. Res. US Geol. Soc.*, **6**(5), 637–649.
- Whipple, K.X. & Tucker, G.E., 2002. Implications of sediment-flux-dependent river incision models for landscape evolution, *J. geophys. Res.*, **107**, B2 2039, doi:10.1029/2000JB000044.
- Whipple, K.X., Kirby, E. & Brocklehurst, S.H., 1999. Geomorphic limits to climate-induced increases in topographic relief, *Nature*, **401**, 39–43.
- Willett, S.D., Beaumont, C. & Fullsack, P., 1993. Mechanical model for the tectonics of doubly vergent compressional orogens, *Geology*, **21**, 371–374.
- Willett, S.D., Fisher, D., Fuller, C., Yeh, E.C. & Lu, C.Y., 2003. Erosion rates and orogenic wedge kinematics in Taiwan inferred from apatite fission track thermochronometry, *Geology*, **31**, 945–948.
- Wu, F.-T., 1978. Recent tectonics of Taiwan, *J. Phys. Earth*, **26**, S265–S299.

- Yu, S.B. & Kuo, L. C., 2001. Present-day crustal motions along the Longitudinal Valley Fault, eastern Taiwan, *Tectonophysics*, **333**, 199–217.

APPENDIX A: DERIVATION OF ASYMMETRY FACTOR

Refer to Fig. 11(b)

$$h = \frac{w}{\cos \phi}$$

$$x + y = 2w \cos \theta$$

$$x = h \cos(\phi - \theta)$$

$$x = \frac{w \cos(\phi - \theta)}{\cos \phi}$$

$$AF = \frac{x}{x + y} = \frac{\cos(\phi - \theta)}{2 \cos \phi \cos \theta}.$$

Refer to Fig. 11(c)

$$\tan \phi = \frac{b}{s}$$

$$\tan(\phi - \theta) = \frac{b}{x}$$

$$s = \frac{x \tan(\phi - \theta)}{\tan \phi}$$

$$AF = \frac{s}{x + y}$$

$$AF = \frac{x \tan(\phi - \theta)}{\tan \phi} \frac{1}{x + y}$$

$$AF = \frac{w \cos(\phi - \theta) \tan(\phi - \theta)}{\cos \phi \tan \phi} \frac{1}{2w \cos \theta}$$

$$AF = \frac{\cos(\phi - \theta) \tan(\phi - \theta)}{2 \sin \phi \cos \theta}.$$